Semiconductor Science and Technology

PAPER • **OPEN ACCESS**

Continuum level-set model for anisotropic wet etching of patterned sapphire substrates

To cite this article: A Toifl *et al* 2021 *Semicond. Sci. Technol.* **36** 045016

OPEN ACCESS
IOP Publishing
Semiconductor Science and Technology
Semicond. Sci. Technol. **36** (2021) 045016 (12pp)
https://doi.org/10.1088/1361-6641/abe49b

Continuum level-set model for anisotropic wet etching of patterned sapphire substrates

A Toifl[1], F Rodrigues[1], L F Aguinsky[1], A Hössinger[2] and J Weinbub[1]

[1] Christian Doppler Laboratory for High Performance TCAD, Institute for Microelectronics, TU Wien, Gußhausstraße 27-29, 1040 Wien, Austria
[2] Silvaco Europe Ltd Compass Point, St Ives, Cambridge PE27 5JL, United Kingdom

E-mail: alexander.toifl@tuwien.ac.at

Received 20 October 2020, revised 15 January 2021
Accepted for publication 9 February 2021
Published 10 March 2021

Abstract

We present a continuum modeling approach to simulate anisotropic wet etching of single-crystal sapphire employing mixtures of sulfuric acid and phosphoric acid. Wet etching of sapphire leads to the formation of crystal facets with high Miller–Bravais indices. The resulting complex three-dimensional topographies can be exploited to optimize the patterning of sapphire substrates which are employed for gallium nitride based light-emitting diodes. Due to the strong impact of the three-dimensional sapphire topography on the light extraction efficiency of the final device, precise control over the wet etching process, in particular etchant mixture, etch time, and temperature, is highly important. We present our model in the context of process technology computer-aided design, where we use the level-set method to track the evolution of the three-dimensional etch profile over time. In order to describe the intricate anisotropy of wet etched sapphire, we propose a flexible interpolation method for the etch rate distribution, which incorporates experimentally characterized crystal facets and deduces local extrema in the distribution based on local convexity/concavity considerations. The developed model has been calibrated and evaluated based on scanning electron microscopy and atomic force microscopy characterizations from the literature. Our model enables accurate sapphire etching simulations, where the emerging and disappearing crystal facets show a good agreement with experimental observations for several etchant mixtures and temperatures.

Supplementary material for this article is available online

Keywords: anisotropic wet etching of sapphire, patterned sapphire substrates, continuum modeling of etching processes, crystallographic anisotropy, level-set method

(Some figures may appear in colour only in the online journal)

1. Introduction

Anisotropic wet etching of single-crystal sapphire has received much attention in the field of light-emitting diode (LED) manufacturing due to its ability to generate the necessary complex topographies. In particular, gallium nitride (GaN) based LEDs most commonly utilize patterned sapphire substrates (PSS) to enhance the light extraction efficiency (LEE) of the final device [1]. The LEE is strongly impacted by the surface geometry of the PSS [2, 3], which provides a pathway to enhancing the device performance by optimizing the patterning of the sapphire substrates. A variety of geometries, e.g. hemispheres [4] and pyramids [5], have been manufactured. Due to its reliability and simplicity, anisotropic

wet etching of single-crystal sapphire is utilized to engineer the surface topography [6, 7]. Although recent research investigates potassium hydroxide (KOH) [8], the most commonly employed wet etchants consist of mixtures of sulfuric acid H_2SO_4 and phosphoric acid H_3PO_4 [9–14]. The resulting etch profiles are complex geometries with high Miller–Bravais-index crystal facets. The crystallography has been experimentally characterized by several research groups, using atomic force microscopy (AFM) and scanning electron microscopy (SEM) [10, 13]. The time evolution of the etch profile shows distinct emerging and disappearing crystal facets and zones, contributing to a high geometric complexity of the observed sapphire topography. Due to the strong impact on the LEE of the final LED, precise control over the resulting three-dimensional topography is essential.

We present a geometry-focused modeling and simulation approach based on the level-set method, in order to facilitate the optimization of the wet etching step with respect to etch time, temperature, and etchant mixture. Our approach is based on a continuum description of the wet etching process, which is, as will be shown, well suited to describe the emergence of facets with high crystal quality and enables the simulation of large three-dimensional structures. This is in contrast with atomistic or molecular approaches, where microscopic surface features are studied [15–17]. By making use of the surface tracking capability of the level-set method [18], the complex geometric evolution of the substrate during etching can be described and semiconductor fabrication steps can be optimized with an engineering-focused process technology computer-aided design (TCAD) workflow [19, 20]. The level-set method allows for convenient and efficient treatment of topographical changes in three dimensions and for interfacing with other process simulation (e.g. mask formation, dry etching, doping) and device simulation (e.g. LED characteristics) workflows [21]. Rapid incorporation of our model into established TCAD workflows is thus enabled, allowing for further computational investigations.

In the past, the level-set method has been employed for the simulation of wet etching of silicon (Si) with etchants such as KOH or tetramethylammonium hydroxide (TMAH) [22–24]. In these studies, the wet etching process has been modeled by defining an etch rate distribution function that has been specifically tailored to the cubic symmetry of Si and the characteristic low-index planes observed in etching experiments.

Whereas the wet etching of Si is well studied, the etch rate anisotropy of single-crystal sapphire is still being investigated. Several studies measured the etch profile evolution and characterized the crystal facets observed in the experiment [11, 14, 25–28]. In these studies, only a small number of etch rate/crystal direction pairs have been identified, due to the limited number of distinct crystal facets emerging during the etching process. Strikingly, these reported pairs are not consistent throughout these studies. Recently, Xing *et al* presented a comprehensive characterization of etch rates for various etching solutions and temperatures [7], providing additional insights into the etching anisotropy of sapphire. Most importantly, these studies show that the etch rate anisotropy of sapphire is significantly more intricate compared to Si.

Due to the intricate anisotropy, the etch rate distribution functions specifically defined for Si cannot be straightforwardly transferred to sapphire if the number of identified crystal direction is small. Thus, there are two options to achieve high-accuracy level-set models for anisotropic wet etching models of sapphire. The first option is to incorporate elaborate experimental characterization techniques into the model calibration process. This approach has been presented by Zhang *et al* [29], who employ hemisphere etching experiments and, thus, effectively generate a large number of identified pairs of crystal direction and etch rate. In the second approach, it is desired to only use standard characterization data stemming from a limited number of SEM images and AFM measurements. Consequently, more flexible methods to incorporate the etch rates of a given small set of identified characteristic crystal facets and the corresponding etch rates are required to account for the intricate anisotropy of sapphire. In this study, we focus on the second approach and present a continuum level-set modeling methodology which results in calibrated models with a small number of model parameters, but still enables high-accuracy three-dimensional simulations of anisotropic wet etching of sapphire.

This work is organized as follows. In section 2, we present a general interpolation methodology which enables practical modeling of highly anisotropic processes with trigonal symmetry by a level-set method. In section 3, we give a short overview of a comprehensive series of experiments conducted by Shen *et al* [26–28] which lay the groundwork for validating our model. In particular, we show that insights into the etch rate anisotropy can be deduced from geometrical considerations, even if a full characterization of the etchant is not available. In section 4, we employ our recently developed level-set method for multi-material wet etching and non-planar selective epitaxy [20] to conduct three-dimensional simulations for several etchant mixtures and temperatures and compare the results to the experiments presented in section 3, demonstrating good agreement.

2. Modeling anisotropic wet etching

Wet etching of single-crystal sapphire results in topographies characterized by crystal facets. Due to the emergence of high-index facets, complex three-dimensional structures are formed. Even though the microscopic surface morphology depends on the crystallographic orientation [7], the overall surface quality of wet etched sapphire is typically high compared to alternative processing techniques (e.g. plasma etching [30]). Furthermore, the surface topography on the micrometer scale strongly impacts the total internal reflection at the sapphire-GaN interface of the fabricated LED. Continuum modeling of the wet etching process is well suited to describe the evolution of the complex surface topography.

Anisotropic wet etching strongly depends on crystal quality and etchant concentration/mixture ratios. The etching process is controlled by the kinetics of the reaction, resulting in

significant temperature dependence of the etch rates [31–33]. In the particular case of sapphire etched with mixtures of H_2SO_4 and H_3PO_4, Shen *et al* have reported high activation energies (87.0–108.3 kJ mol^{-1}), supporting the reaction-limited characteristics of the etching [28]. Thus, the impact of reactant diffusion can be neglected and the etching reaction can be characterized with the orientation dependence of the etch rate [7], i.e. by assigning every possible crystal direction an unambiguous etch rate for a certain constant temperature.

Within the level-set method we can define a crystal direction-dependent etch rate, represented by a continuous function $V(\vec{n})$ for every possible direction $\vec{n}$ on the unit sphere. $V(\vec{n})$ is incorporated into the level-set equation [18]:

$$\frac{\partial \phi}{\partial t} + V(\vec{n})\vec{\nabla}\phi = 0, \tag{1}$$

which determines the time evolution of the wafer surface (i.e. surface topography). The topography is implicitly described via the level-set function $\phi = \phi(x, y, z, t)$, which is a function of the spatial coordinates and time. After the starting topography (e.g. conically shaped sapphire substrates) is set via the initial value of the level-set function $\phi(x, y, z, t_0)$, the discretized version of equation (1) is solved with given $V(\vec{n})$ to calculate the evolved topography $\phi(x, y, z, t_0+\Delta t)$. Numerical details of the discretization are discussed in [20], where a stable and robust level-set method for anisotropic fabrication processes is presented. With this numerical method, modeling the anisotropic wet etching of sapphire is possible by constructing $V(\vec{n})$ based on experimental data.

Typically, only a limited number of precisely identified etch rates is available from experiments. This is due to the small number of dominating facets appearing during etching. These facets are the only source for reliable measurements of etch rates for a given crystal direction. In order to define a continuous $V(\vec{n})$, an interpolation scheme has to be employed. Most importantly, $V(\vec{n})$ is required to respect the crystal symmetry of the material to be etched (trigonal symmetry in the case of sapphire). In the following, an approach to account for the symmetry is presented.

2.1. Incorporating trigonal symmetry

Due to the symmetry of single-crystal materials, crystallographically equivalent planes show the same etch rates [34]. As a consequence, the etch rate model $V(\vec{n})$ has to reflect the crystal symmetry. While the well-established Si crystal shows hexoctahedral symmetry in the cubic crystal system, sapphire exhibits ditrigonal scalenohedral symmetry in the trigonal system (crystal class D_{3d} in Schönflies notation or, equivalently, $\bar{3}$m in Hermann–Mauguin notation) [35, 36].

In order to reflect the crystal symmetry, we consider the fundamental domain F of the crystal symmetry, which is a subset of crystal directions [37]. If the etch rate is known for every direction $\vec{n}_F$ in the fundamental domain, the etch rate for every possible direction $\vec{n}$ on the unit sphere can be inferred. For a given general $\vec{n}$, symmetry operations associated with the crystal class can be employed to map $\vec{n}$ to the crystallographically equivalent $\vec{n}_F$ residing in the fundamental domain. The mapping $\vec{n} \rightarrow \vec{n}_F$ is referred to as *reduction to the fundamental domain* in the following. The fundamental domain of sapphire (crystal class D_{3d}) is the spherical triangle illustrated in figure 1 [37]. Thus, the crystal symmetry is incorporated by applying a sequence of symmetry operations to map all

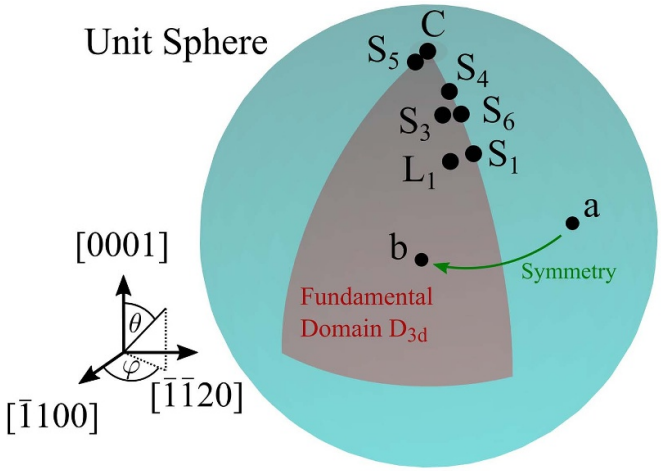

Figure 1. Crystal directions and fundamental domain of the crystal class D_{3d} illustrated on the unit sphere. The crystal directions indicated with C, L_1, S_1, S_3, S_4, S_5, and S_6 indicate characteristic directions related to the wet etching of sapphire and reside within the fundamental domain. We choose the nomenclature of crystal directions based on [26] to simplify the discussion in section 4. The general direction 'a' can be reduced to the crystallographically equivalent direction 'b' within the fundamental domain by employing a series of D_{3d} symmetry operations.

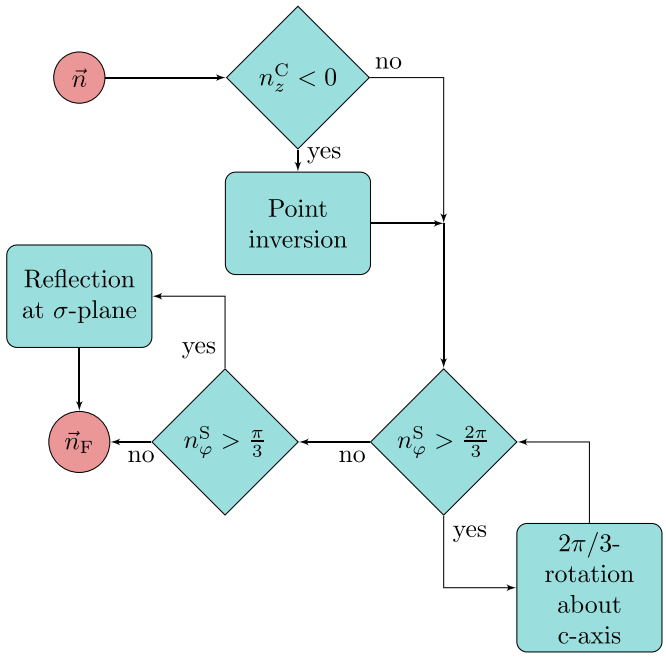

Figure 2. Flowchart of the algorithm to reduce a general direction $\vec{n}$ to the equivalent direction $\vec{n}_F$ residing in the D_{3d} fundamental domain. The employed coordinate system is shown in figure 1. n_z^C refers to the z component of the Cartesian representation of $\vec{n}$ and n_φ^S denotes the polar angle of $\vec{n}$ in spherical coordinates.

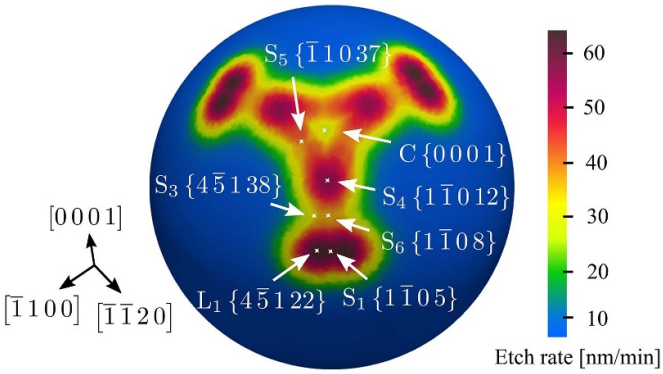

Figure 3. Visualization of an etch rate distribution constructed with equation (2). The model parameters are calibrated to reflect the etchant solution H_2SO_4:H_3PO_4 = 3:1 at 503 K (further discussed in section 4). The crystal directions corresponding to the facets C, S_1, etc are shown and their significance for sapphire etching is discussed in section 3.2.

directions to F. For sapphire's D_{3d} symmetry we employ a reduction algorithm, which is illustrated in figure 2 and is based on a combination of point inversion, $2\pi/3$-rotation about the c-axis, and reflection at the σ-plane[3]. After the reduction procedure, all directions on the unit sphere are mapped to F. Therefore, it is sufficient to define the etch rate distribution on F. As a consequence, the etch rate interpolation is facilitated, as described in the following section.

2.2. Interpolation method

An interpolation method to reconstruct the continuous etch rate distribution $V(\vec{n})$ is required, because typically only a limited number of defined crystal facets are experimentally characterized [10, 13]. The standard approach is to perform trilinear interpolation between the experimental data points [33, 38]. However, this approach requires a large number of known etch rates for given crystal directions to model an intricate distribution with several local minima and maxima as it is prevalent for sapphire etching [7]. Figure 3 shows the typical $V(\vec{n})$ constructed based on experiments by Shen *et al* [26] with distinct local maxima and minima.

We employ an interpolation approach based on the parametrization:

$$V(\vec{n}) = V_0 + \sum_i \alpha_i \langle \vec{n}, \vec{m}_i \rangle^{\omega_i} \mathrm{H}(\langle \vec{n}, \vec{m}_i \rangle), \qquad (2)$$

which is structurally similar to the parametrization proposed by Siem and Carter in the context of thermodynamic surface free energy calculation [39] and has also been used in the field of phase-field growth simulation [40, 41]. V_0 refers to an isotropic distribution, which is extended by a sum of power cosine distributions, each centered around a given crystal direction $\vec{m}_i$, where H is the Heaviside function and $\langle \cdot, \cdot \rangle$ indicates the scalar product. Thereby, spatially confined extrema determined by the coefficients α_i and $\omega_i > 0$ are constructed. α_i can be calculated from given etch rates R_i by solving the linear system $V(\vec{m}_i) = R_i$. The distribution presented in figure 3 is generated with this parametrization and is characterized by a combination of an isotropic contribution and several minima/maxima added at specific crystal directions indicated by S_1, S_3, etc. Compared to the trilinear interpolation approach, equation (2) enables control of the extrema even for a small number of known etch rate/crystal direction pairs. Furthermore, as no triangulation is required, it is not necessary to include supplemental rates at the boundary of the fundamental domain[4]. In summary, equation (2) enables reconstruction of the etch rate distribution, particularly in presence of a limited number of characterized crystal facets.

3. Anisotropic wet etching of sapphire

In this section, we focus on the practical aspects of modeling the anisotropic wet etching of PSS, employing the techniques presented in section 2. A comprehensive study by Shen *et al* [26–28] serves as the experimental reference for our modeling approach. First, we discuss the experimental setup and the implications for modeling the etching process. Second, we present a method to construct the etch rate distribution based on the characterization information provided by typical sapphire etching experiments.

3.1. Experimental setup

Shen *et al* presented a study of the geometric evolution of PSS during an anisotropic wet etching step [26–28]. The c-plane substrate was pre-patterned to fabricate an array of cones with hexagonal symmetry (3.2 μm pitch). The base diameter of the individual cones was 2.93 μm. The array served as the initial topography which was etched with several mixtures of H_2SO_4 and H_3PO_4 at various temperatures. The etchant solutions were referred to as MX-Y, where X-Y indicates a volume ratio of H_2SO_4:H_3PO_4 = X:Y. The topography was characterized with SEM and AFM. The several crystal facets that appeared during the etching process were identified and their Miller–Bravais indices were determined. The evolution of topography was documented for a plethora of etch times, with one example shown in figure 4 (originally published in [27]). Additionally, high activation energies of the etching reaction were confirmed, indicating reaction-limited reactions [26–28].

The reaction-limited nature of the etching process motivates our main modeling assumption: The etch rate depends only on the crystal facets locally exposed to the etchant. Therefore, an etch rate distribution $V(\vec{n})$ can be defined and is valid for a processing temperature T and an etchant mixture MX-Y. However, for the various processing conditions only three to four reliably identifiable crystal facets appearing during the etching process were characterized. Nevertheless,

[3] The σ-plane is spanned by $[\bar{1}100]$ and $[0001]$.

[4] This ensures that the fundamental domain is fully covered with triangles, which is necessary to perform trilinear interpolation for every point in the fundamental domain.

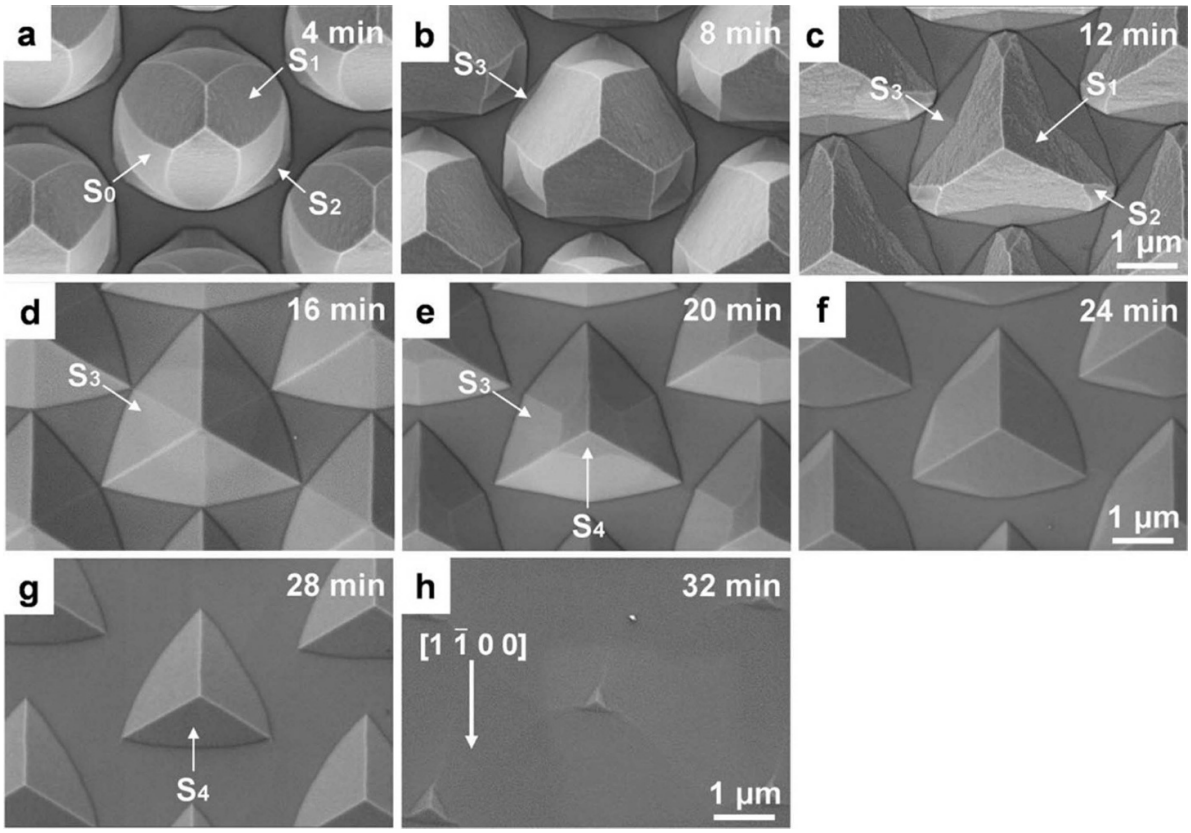

Figure 4. SEM images of the topography of sapphire during wet etching employing H_2SO_4:H_3PO_4 = 3:1 at 503 K, as published by Shen *et al* [27] (figure 2) under Creative Commons Attribution 4.0 License (http://creativecommons.org/licenses/by/4.0/).

the geometric features during the evolution of the topography enable the reconstruction of $V(\vec{n})$ with high accuracy, as presented in the following section.

3.2. Constructing the etch rate distribution

Figure 4 shows SEM images of the typical topographical evolution of the PSS during wet etching. Starting with the initial cone shape (S_0), a crystal facet S_1 with very high etch rates *immediately* emerges near the apex (a). After 8 min a slower etching facet S_3 can be observed at the base. As etching proceeds, S_3 fully replaces S_1 (d). However, there is another facet S_4 emerging at the top of the structure, eventually dominating (f) before the entire initial topography is etched away. All experiments presented by Shen *et al* show a similar sequence of facets appearing at the apex and the base, until the c-plane wafer surface becomes predominant again.

We can use the information of the topographical evolution to predict structural properties of the etch rate distribution $V(\vec{n})$. In particular, the local convexity of the topography is significant. Figure 5 shows an illustration of the cross-section of the experiment for several etch times. The cone's apex locally constitutes a convex region, whereas the base forms a concave region. In a convex region the rapidly etching facets ('fast planes') dominate the topography evolution and in a concave region the slowly etching facets ('slow planes') define the geometry [42]. Equivalent geometric properties have been

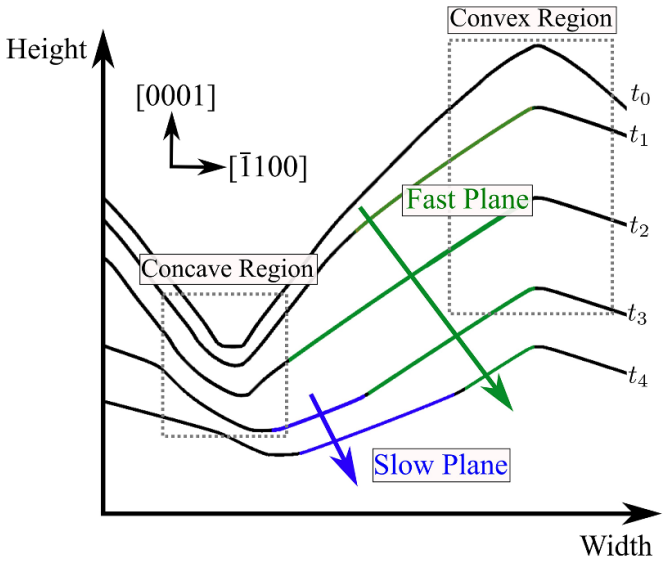

Figure 5. Illustration of the etch profile evolution for a highly anisotropic etching process. In locally convex regions fast etching planes dominate, whereas in locally concave regions slowly etching planes remain and become observable.

studied in the context of kinetically-limited anisotropic crystal growth [43]. We can thus deduce that facets appearing in a convex region are etched faster than all neighboring facets with

similar Miller indices. $V(\vec{n})$ has necessarily a *local maximum* at the corresponding direction. Analogously, a facet appearing in concave region requires $V(\vec{n})$ to have a *local minimum* at this facet's normal vector $\vec{n}$. Therefore, the etch rates of facets S_1 and S_4 constitute local maxima in $V(\vec{n})$, while facet S_3 is a local minimum (see figure 3). The incorporation of this structural information greatly facilitates the calibration process of the etching model $\vec{n}$ and enables high-quality initial guesses of etch rates for crystal facets, even if the exact rate has not been determined.

4. Results and discussion

In this section, we employ our modeling approach to simulate and analyze the sapphire topography evolution investigated in the experiments presented by Shen *et al* [26–28]. This set of SEM images and AFM data has been chosen since all experimental results originate from the same setup. Additionally, the data set features a broad range of etchant mixtures, etch temperatures, and times. Our approach has been implemented into the TCAD process simulator Silvaco Victory Process [44] and the etching simulation presented here is based on the Stencil Lax-Friedrichs method [20] which enables numerically stable simulations of strongly anisotropic processes. Furthermore, in order to focus on the wet etching step, we have set up the pre-patterned cones based on the AFM data presented by Shen *et al* [26].

Due to the reaction-limited *nature* of the wet etching process we employ an etch rate distribution $V(\vec{n})$, valid for a certain process temperature T and etchant mixture of H_2SO_4 and H_3PO_4. Additionally, we assume stable process conditions such that $V(\vec{n})$ does not change over time. In the following sections, we present the calibration and validation procedure for $V(\vec{n})$ (section 4.1) and discuss the results of our simulation study (section 4.2).

4.1. Model calibration and verification

In the first step, the basic properties of $V(\vec{n})$ are determined by following the approach described in section 3.2. Here, the crystal directions $\vec{n}$ which constitute the local extrema of $V(\vec{n})$ are identified using the experimental facet characterization by Shen *et al* In particular, the Miller–Bravais indices of the emerging crystal facets (S_1, S_3, S_4, S_5, and S_6) have been determined by Shen *et al* and serve as the foundation for our model. The Miller–Bravais indices $(ijkl)$ of a facet are converted to the Cartesian representation of the facet normal vector [45]:

$$\vec{n} = h\vec{a}_1 + k\vec{a}_2 + (-h-k)\,\vec{a}_3 + \frac{3}{2}\frac{a^2}{c^2}l\vec{c}, \quad |\vec{a}_{\{1,2,3\}}| = a, \quad |\vec{c}| = c, \tag{3}$$

where we assume the lattice constant ratio c/a as 12.991 Å/4.785 Å. $\vec{a}_1$, $\vec{a}_2$, and $\vec{a}_3$ reside within the c-plane and $\vec{c}$ is perpendicular to the c-plane. Additionally, the trigonal symmetry is incorporated by employing the approach discussed in section 2.1. In the second step, $V(\vec{n})$ is fine-tuned by calibrating the free model parameters (see also section 2.2) with respect to AFM data and SEM images presented by Shen *et al* [26–28]. Table 1 visualizes all combinations of process temperatures and etchant mixtures (referred to as *etching experiments* in the following) which have been investigated by Shen *et al*. While SEM images are available for eleven etching experiments, a set of AFM profiles consisting of multiple etch times is only presented for M3-1 at 503 K. For all etching experiments, multiple SEM images are provided for several etch times. Thus, the calibration target is to achieve the best possible visual congruence between the simulation result and the SEM images for all available etch times. Additionally, we analyze the local surface normals of our level-set topography description to confirm the emergence of the correct crystal facets in our simulations. Importantly, since the SEM images show the topography from a top view, the etch rate of the c-plane substrate cannot be unambiguously determined. We, therefore, use the experimentally measured c-plane etch rates [27] as a reference in order to ensure that in our model the c-plane etches with the correct rate. The c-plane etch rates have been measured by Shen *et al* with high accuracy using the technique of masked plane sapphire substrates [27].

Table 1. Summary of etch rate experiments conducted by Shen *et al* [26–28], which are the reference experiments for the calibration of our model. The symbol × denotes that Shen *et al* have presented SEM images and the symbol ◯ indicates that a set of AFM profiles consisting of multiple etch times is available.

	Temperature (K)			
Etchant	473	503	523	543
M5-1	×	×	×	×
M3-1		×◯		
M1-1		×		
M1-3		×		
M0-1	×	×	×	×

We demonstrate and validate the calibration procedure with the etching experiment M3-1 at 503 K. In the experiments, Shen *et al* have characterized three crystal facets: $S_1\{1\bar{1}05\}$, $S_3\{4\bar{5}138\}$, $S_4\{1\bar{1}012\}$. Based on the topographical information, as discussed in section 3.2, we deduce that $V(\vec{n})$ necessarily needs to have a local minimum along S_3 and local maxima along S_1 and S_4. The experimentally observed topography evolution (figure 4) shows the immediate formation of S_1. This implies that the etch rate of S_1 (R_1) is greater than or equal to the etch rate of S_4 (R_4), because otherwise S_4 would emerge near the top of the cone. With these boundary conditions, we calibrate the model parameters based on the congruence of SEM image and simulation results. The resulting parameters for the calibrated model are shown in table 2. We achieved the best congruence for the entire etch profile evolution by broadening the maximum along S_1. In particular, the broadening is essential for the formation of the subsequently appearing facet S_3. In the experimental study by Xing *et al* [7] broadened maxima have been reported for etchants M1-1 and M3-1 as well

Table 2. Model parameters for etchant mixtures M3-1, M1-1, and M1-3. The columns refer to the directions which are used in the parametrization equation (2) and also include the isotropic component V_0.

M3-1	$T = 503$ K	Directions					
		C	S_1, L_1	S_3	S_4	S_5	V_0
	Weights ω	200	100	60	100	100	
	Etch rates R (nm min^{-1})	24	59	36	57	39	8
M1-1	$T = 503$ K	Directions					
		C	S_1, L_1	S_3	S_4	S_5	V_0
	Weights ω	200	100	60	100	100	
	Etch rates R (nm min^{-1})	18	60	37	52	36	7
M1-3	$T = 503$ K	Directions					
		C	S_1, L_1	S_3	S_4	S_5	V_0
	Weights ω	200	100	60	100	100	
	Etch rates R (nm min^{-1})	16	62	39	51.5	34	8

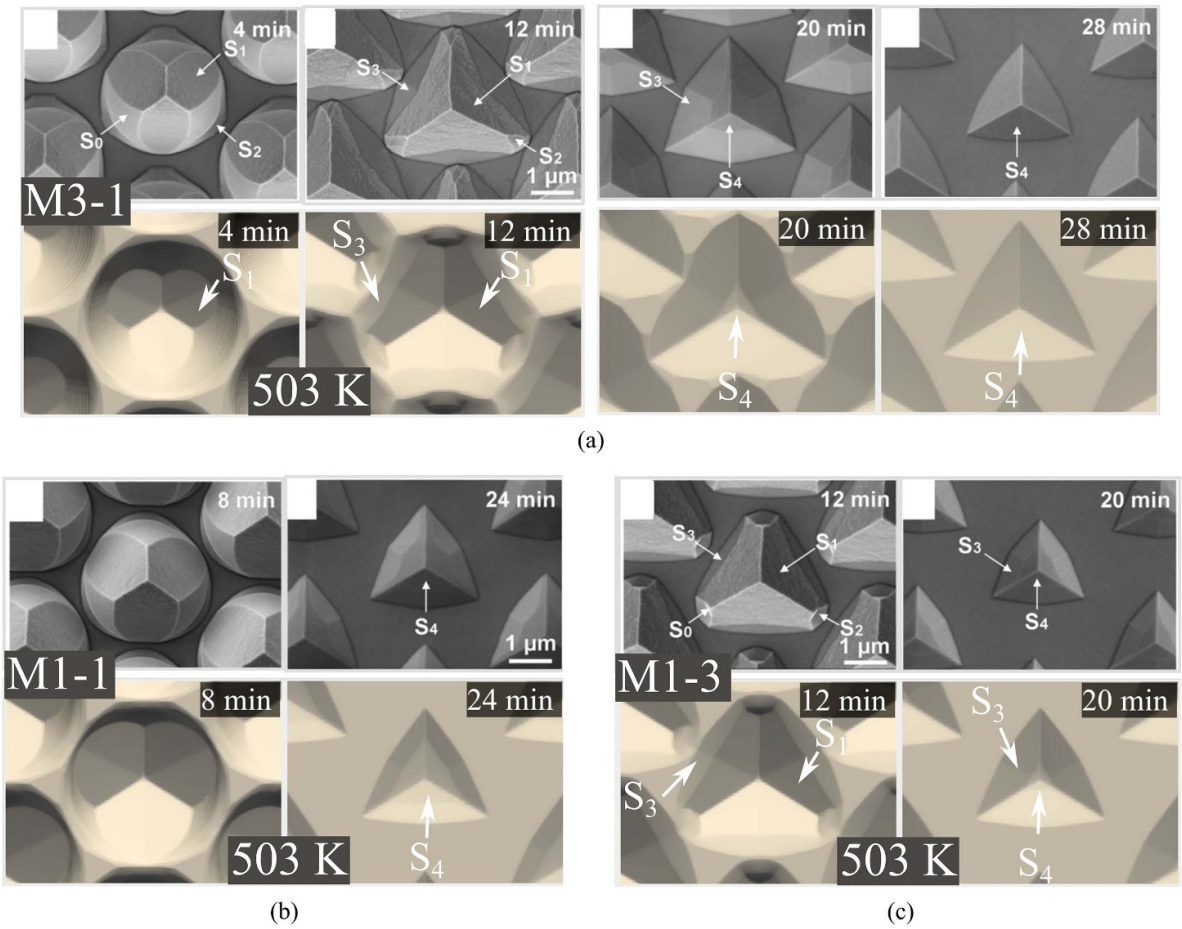

Figure 6. Comparison of the SEM images (top) with the simulation results (bottom) for different etch times and etchant mixtures. (a) M3-1 at 503 K, (b) M1-1 at 503 K, (c) M1-3 at 503 K. Similar comparisons are provided for all available etch times and temperatures as supplemental material (available online at stacks.iop.org/SST/36/045016/mmedia). The SEM images were published by Shen *et al* [27] (figures 2, 5 and 6) under Creative Commons Attribution 4.0 License (http://creativecommons.org/licenses/by/4.0/).

at the slightly different etching temperature of 509 K. Thus confirming that the broadening is an essential physical effect which needs to be reflected in our models. In order to comply with our objective to keep the model complexity at a minimum, the broadening is implemented by incorporating only one additional direction L_1 which corresponds to a $\{4\bar{5}122\}$ facet. The associated etch rate is set to $R_{L1} = R_1$, i.e. no additional rate parameter is introduced. The contributions of the two terms corresponding to S_1 and L_1 in equation (2) superposeto create the broadened maximum shown in the

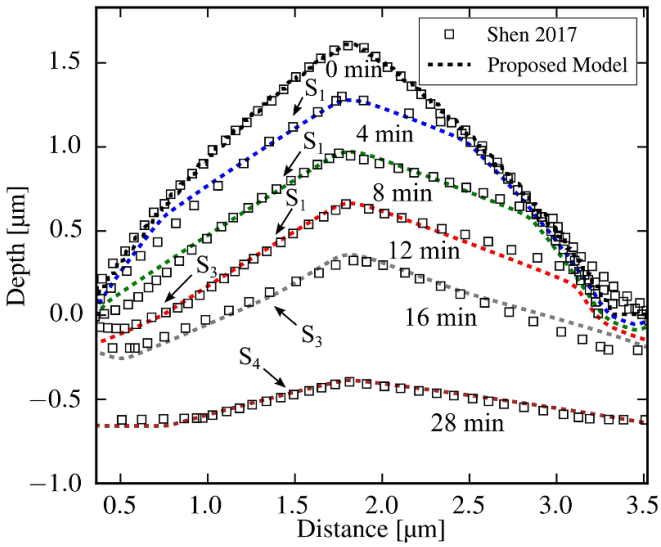

Figure 7. Comparison of AFM data [26] and simulation results for the etchant M3-1 at 503 K. On the left half of the illustrated cone profile the crystal facets S_1, S_3, and S_4 can be observed, while the right half outlines ridges of the topography where two crystallographically equivalent topography zones coincide.

visualization of $V(\vec{n})$ in figure 3. Furthermore, we include a direction corresponding to $S_5\{\bar{1}1037\}$, which is a facet that has been characterized by Shen *et al* for M5-1 experiments and ensures that the c-direction $[0001]$ constitutes a local minimum. This is motivated by the fact that all other facets are eventually etched away and the c-plane remains. Additionally, the inclusion of S_5 is again consistent with the characterization presented in [7].

The resulting etching simulations for etchant mixture M3-1 are compared with SEM images in figure 6(a), indicating congruence over the entire range of available etch times 4–28 min). In order to validate the modeling approach, we consider the two-dimensional etch profiles of the PSS along $[\bar{1}100]$ (see figure 7). Good agreement of the simulated profiles with the experimental observations is demonstrated. Consequently, we conclude that optimization of visual congruence and incorporating the experimental values for R_C results in suitable expressions for $V(\vec{n})$. We thus repeat the calibration procedure to construct $V(\vec{n})$ for etchant mixtures M1-1 and M1-3 at 503 K. The corresponding parameters and simulation results are presented in table 2, and figures 6(b) and (c), respectively. Most importantly, the resulting models are characterized by the same set of directions and the exact same values for the weights ω_i.

The etch experiments for M0-1 and M5-1 are particularly interesting, because Shen *et al* have presented SEM images for several temperatures (473, 503, 523, and 543 K). The experiments exhibit a structural difference between the H_3PO_4 solution (M0-1) and the mixture M5-1 [28]. The former results in the formation of a facet $S_6\{1\bar{1}08\}$ instead of S_3, whereas the latter exhibits a topography evolution which is similar to the etchants discussed above. For the H_3PO_4 solution, S_4 facets have not been observed for any of the investigated temperatures. By resorting to the topography evolution argument, we conclude that the corresponding R_6 constitutes a local minimum, where the R_6 is only slightly smaller than the local maximum R_4. As a result, S_6 is etched away before S_4 evolves from the convex top of the structure. Based on this premise, the calibrations result in high accuracy models with parameters summarized in table 3 and topography comparisons depicted in figures 8(a) and (b).

With $V(\vec{n})$ calibrated for four different temperatures, we investigate the temperature dependence of the model etch rates R_i and the isotropic component V_0. Figure 9 shows the etch rate distributions and the etch rates in a semi-logarithmic Arrhenius plot. First, we achieved accurate results by using the same set of weights ω_i for all temperatures. This indicates that there is a fundamental temperature-independent form $V(\vec{n})$. Second, the M5-1 model is characterized by the same ω_i as the M3-1, M1-1, and M1-3 models. Third, the etch rates of M0-1 and M5-1 exhibit a temperature dependence that is properly captured by an Arrhenius law

$$R = A \exp\left(-\frac{E_a}{k_B T}\right), \tag{4}$$

where R is the etch rate (also including the isotropic component V_0), A is a pre-exponential coefficient, E_a is the activation energy in eV, k_B is the Boltzmann constant, and T is the etching temperature. The Arrhenius plots depicted in figures 9(b) and (d), respectively, show that all R_i and V_0 follow an Arrhenius law. The pre-exponential coefficients and activation energies are determined employing standard Arrhenius law fitting and the resulting values are given in table 3.

4.2. Discussion

We assembled continuum sapphire etching models for all etching experiments indicated in table 1 by employing the calibration procedure presented in the previous section. In this section, we examine the temperature dependence and discuss the applicability of our models.

The etch rates of mixtures M0-1 and M5-1 are characterized by high activation energies $E_a > 0.85$ eV in the temperature range [473, 543 K]. This is consistent with the assumption of reaction-limited etching and solidifies the modeling approach with a crystal orientation-dependent etch rate distribution $V(\vec{n})$. As evident from figure 9, the etch rate values of the defining crystal directions S_1, S_3, etc are all in the same order of magnitude (for constant temperature). At the same time the etch rate distribution is complex, due to the multiple local extrema. Additionally, the defining crystal directions all reside in a section that is smaller than a quarter of the fundamental domain (see figure 1). As a consequence, the evolving crystal facets have similar Miller–Bravais indices, which contributes to the intricate etch anisotropy of sapphire. The determined Arrhenius parameters for all etch rates enable high-quality etching models for etchants M0-1 and M5-1 for any temperature within [473, 543 K].

Furthermore, with the exception of the isotropic component V_0, the activation energies of the defining crystal rates are differing less than 10%. Due to the small difference, the order

Table 3. Model parameters for etchant mixtures M0-1, and M5-1. The columns refer to the directions which are used in the parametrization equation (2) and also include the isotropic component V_0. The etch rates are modeled using the Arrhenius law equation (4) with parameters A and E_a.

M0-1	Directions					
	C	S_1	S_4	S_5	S_6	V_0
Weights ω	200	100	100	100	100	
A (nm min^{-1})	5.296×10^{10}	4.897×10^{10}	6.953×10^{10}	1.407×10^{10}	8.894×10^{10}	3.236×10^{11}
E_a (eV)	0.962	0.882	0.909	0.862	0.923	1.054
M5-1	**Directions**					
	C	S_1, L_1	S_3	S_4	S_5	V_0
Weights ω	200	100	60	100	100	
A (nm min^{-1})	1.667×10^{11}	7.551×10^{11}	5.378×10^{11}	6.444×10^{11}	9.042×10^{11}	5.444×10^{12}
E_a (eV)	0.974	1.018	1.021	1.011	1.039	1.152

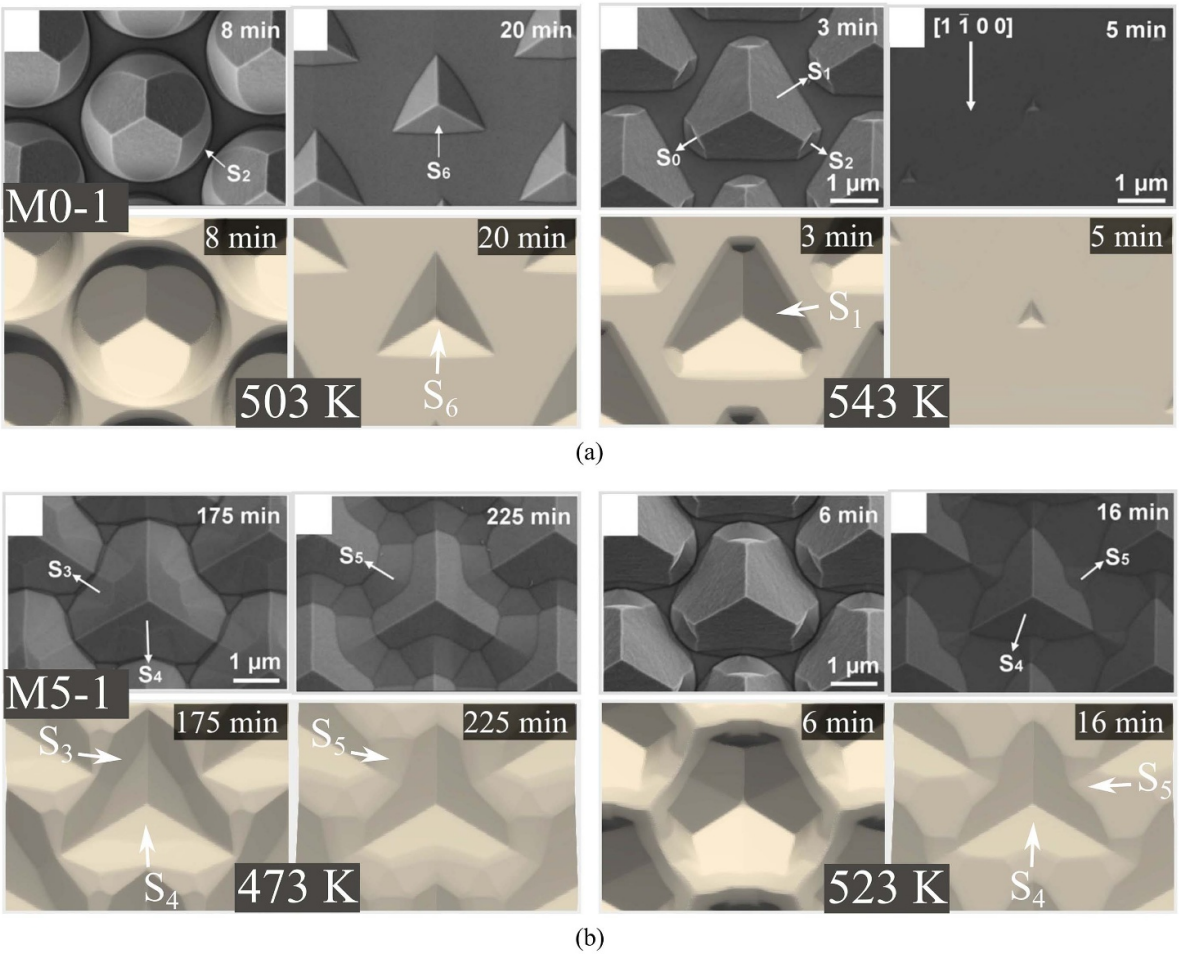

Figure 8. Comparison of SEM images (top) with the simulation results (bottom) for different etch times and etchant mixtures. (a) M0-1 at 503 and 543 K, (b) M5-1 at 473 and 523 K. Similar comparisons are provided for all available etch times and temperatures as supplemental material. The SEM images were published by Shen *et al* [28] (figures 1, 3 and 7) and [27] (figure 7) under Creative Commons Attribution 4.0 License (http://creativecommons.org/licenses/by/4.0/).

of appearing and disappearing crystal facets remains the same for different temperatures. Accordingly, our model does not show intersections of the Arrhenius line in temperature range [473, 543 K]. However, in the case of M5-1, extrapolation below 473 suggests a crossing of etch rates, which implies a reordering of etch rate values and, consequently, affects the local extrema. Based on the discussion in section 3.2, the local extrema strongly impact the topography evolution. Thus, it is beneficial to identify these crossing points which is now possible with our model.

The details of the presented models (i.e. crystal facets, trigonal symmetry, etch rates and weight coefficients)

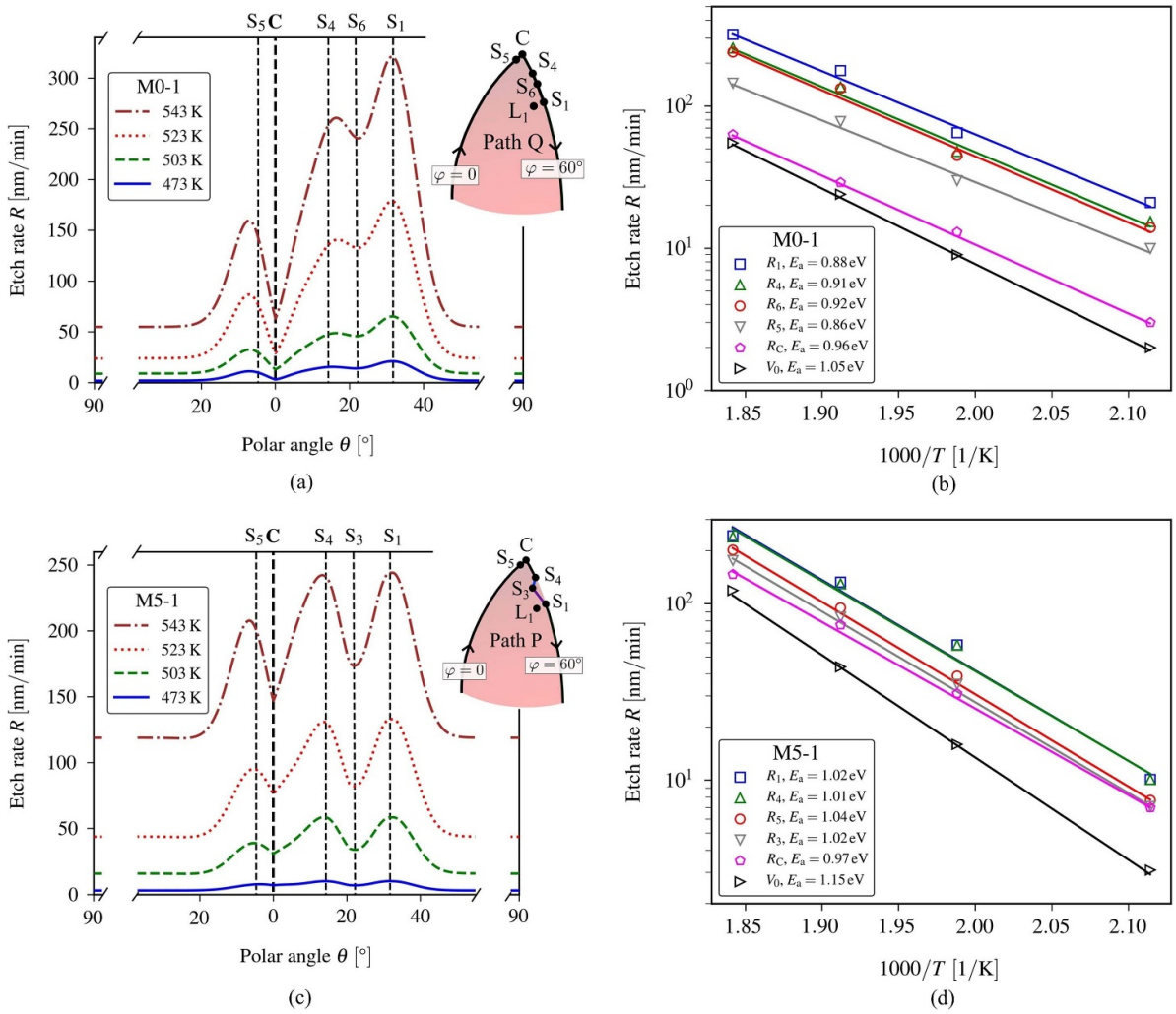

Figure 9. Schematic illustration of the etch rates are along a path illustrated in the inset for etchant mixture (a) M0-1 and (c) M5-1. The etch rates follow Arrhenius law equation (4) and are depicted on a semi-logarithmic scale for etchant mixture (b) M0-1 and (d) M5-1.

are specific for sapphire and the corresponding mixture M0-1 or M5-1. However, the general methodology consisting of identifying characteristic crystal directions, deducing information from considering the convexity and employing parametrization equation (2) can also be transferred to reaction-limited wet etching of other materials. If a substrate material with a different crystal structure is considered, the details of the algorithm *reduction to the fundamental domain* have to be adapted to account for the applicable crystal symmetry. If wet etching of sapphire with other etchants is considered, the set of crystal facets and the corresponding model coefficients are potentially different (see table 3), but the general methodology of sections 2 and 3 can also be applied in this case.

As has been shown, the topographies resulting from an etching process not only depend on the properties of the etchant, but also on the initial topography configuration (e.g. initial cone structures or presence of etching masks). Calibrated continuous etch rate distribution functions $V(\vec{n})$ are advantageous from an engineering point of view, because they can be directly incorporated into the level-set method, ultimately enabling the investigation of the resulting etching profiles as a function of etch mixture, time, temperature, and initial sapphire and etching mask topographies. Furthermore, the geometry-based modeling approach allows for optimization of the device structures which are based on PSS. In particular, the impact of the three-dimensional sapphire topography on the LEE of GaN-based LEDs can be investigated.

5. Summary

We presented an accurate continuum modeling approach for wet etching of sapphire, which considers the intricate anisotropy of sapphire. Our approach enables the construction of etch rate distribution models when only a limited number of etch rates for specific crystal directions is available. This is achieved by integrating basic topographical observations of crystal facets emerging in locally convex and concave regions of the substrate. The applicability of the approach has been demonstrated by predicting the evolution of the three-dimensional etch profiles for a PSS etching experiment

presented by Shen *et al* [26–28]. Our modeling of the etch rate distribution enables high-accuracy simulation results, where the emerging and disappearing crystal facets show a good fit with the experimental observations for several etchant mixtures and temperatures. Notably, the model features distinct minima and maxima in the etch rate distribution, which are consistent with recently published experimental characterizations [7]. Furthermore, we have determined Arrhenius laws for the etch rates of the etchant mixture H_2SO_4:H_3PO_4 = 5:1 and H_3PO_4 solution. Thus, our model enables the prediction of the etch rate magnitude for the topography-defining crystal facets in a range of etching temperatures. The continuum model presented in this work enables TCAD-based optimization of PSSs, being particularly important for tuning LED design and fabrication workflows with respect to the required three-dimensional final geometry, etchant mixture, etch time, and temperature.

Acknowledgments

The financial support by the Austrian Federal Ministry for Digital and Economic Affairs and the National Foundation for Research, Technology and Development is gratefully acknowledged. The authors acknowledge TU Wien Bibliothek for financial support through its Open Access Funding Program.

ORCID iDs

A Toifl https://orcid.org/0000-0001-5054-4477
F Rodrigues https://orcid.org/0000-0002-1594-4966
L F Aguinsky https://orcid.org/0000-0003-4722-0636
A Hössinger https://orcid.org/0000-0002-8949-1680
J Weinbub https://orcid.org/0000-0001-5969-1932

References

[1] Tadatomo K 2017 Epitaxial growth of GaN on patterned sapphire substrates *III-Nitride Based Light Emitting Diodes and Applications* (Singapore: Springer) pp 69–92
[2] Lee T X, Gao K F, Chien W T and Sun C C 2007 *Opt. Express* **15** 6670–6
[3] Keraly C L, Kuritzky L, Cochet M and Weisbuch C 2017 Ray tracing for light extraction efficiency (LEE) modeling in nitride LEDs *III-Nitride Based Light Emitting Diodes and Applications* (Singapore: Springer) pp 301–40
[4] Lee J H, Oh J T, Park J S, Kim J W, Kim Y C, Lee J W and Cho H K 2006 *Phys. Status Solidi* C **3** 2169–73
[5] Li X F, Huang S W, Lin H Y, Lu C Y, Yang S F, Sun C C and Liu C Y 2015 *Opt. Mater. Express* **5** 1784–91
[6] Lee Y J, Hwang J M, Hsu T C, Hsieh M H, Jou M J, Lee B J, Lu T C, Kuo H C and Wang S C 2006 *IEEE Photonics Technol. Lett.* **18** 1152–4
[7] Xing Y, Guo Z, Gosálvez M A, Wu G and Qiu X 2020 *Sensors Actuators* A **303** 111667
[8] Zhang L *et al* 2020 *J. Cryst. Growth* **552** 125926
[9] Cuong T V, Cheong H S, Kim H G, Kim H Y, Hong C H, Suh E K, Cho H K and Kong B H 2007 *Appl. Phys. Lett.* **90** 131107
[10] Yang D *et al* 2014 *Appl. Surf. Sci.* **295** 26–30
[11] Aota N, Aida H, Kimura Y, Kawamata Y and Uneda M 2014 *ECS J. Solid State Sci. Technol.* **3** N69–74
[12] Zhou S, Wang H, Lin Z, Yang H, Hong X and Li G 2014 *Japan. J. Appl. Phys.* **53** 025503
[13] Shen J, Zhang D, Zhang F H and Gan Y 2018 *Appl. Surf. Sci.* **433** 358–66
[14] Sun C, Hui Zhang Y, Xin Zheng Y, Shuang Chu C, Kai Tian K, Fan C, Hui Zhang Z and Bi W 2019 *J. Micromech. Microeng.* **29** 035012
[15] Gosálvez M A, Ferrando N, Fedoryshyn Y, Leuthold J and McPeak K M 2016 *J. Micromech. Microeng.* **26** 045013
[16] Zhang H, Xing Y, Li Y, Gosálvez M A and Qiu X 2017 *Sensors Actuators* A **256** 24–34
[17] Wu G and Xing Y 2020 *J. Microelectromech. Syst.* **29** 1234–44
[18] Osher S and Fedkiw R 2003 *Level Set Methods and Dynamic Implicit Surfaces* (New York: Springer)
[19] Xing Y, Qian J, Gosálvez M A, Zhang J and Zhang Y 2020 *Microelectron. Eng.* **231** 111375
[20] Toifl A, Quell M, Klemenschits X, Manstetten P, Hössinger A, Selberherr S and Weinbub J 2020 *IEEE Access* **8** 115406–22
[21] Klemenschits X, Selberherr S and Filipovic L 2018 *Micromachines* **9** 631
[22] Radjenović B, Radmilović-Radjenović M and Mitrić M 2010 *Sensors* **10** 4950–67
[23] Montoliu C, Ferrando N, Gosálvez M, Cerdá J and Colom R 2013 *Comput. Phys. Commun.* **184** 2299–309
[24] Toifl A, Quell M, Hössinger A, Babayan A, Selberherr S and Weinbub J 2019 Novel numerical dissipation scheme for level-set based anisotropic etching simulations *Proc. Int. Conf. Simulation of Semiconductor Processes and Devices (SISPAD)* pp 327–30
[25] Chen Y C, Lin B W, Hsu W C and Wu Y S 2014 *Mater. Lett.* **118** 72–5
[26] Shen J, Zhang D, Wang Y and Gan Y 2016 *ECS J. Solid State Sci. Technol.* **6** R24–34
[27] Shen J, Zhang D, Wang Y and Gan Y 2017 *ECS J. Solid State Sci. Technol.* **6** R122–30
[28] Shen J, Zhang D, Wang Y and Gan Y 2017 *ECS J. Solid State Sci. Technol.* **6** R163–9
[29] Zhang J, Xing Y, Gosálvez M A, Qiu X, Lin X and Zhang C 2019 Level set simulation of surface evolution in anisotropic wet etching of patterned sapphire substrate *Proc. 32nd Int. Conf. Micro Electro Mechanical Systems (MEMS)* pp 361–4
[30] Donnelly V M and Kornblit A 2013 *J. Vacuum Sci. Technol.* A **31** 050825
[31] Mileham J R, Pearton S J, Abernathy C R, MacKenzie J D, Shul R J and Kilcoyne S P 1995 *Appl. Phys. Lett.* **67** 1119–21
[32] Stocker D A, Schubert E F and Redwing J M 1998 *Appl. Phys. Lett.* **73** 2654–6
[33] Gosálvez M A, Pal P and Sato K 2011 *J. Micromech. Microeng.* **21** 105018
[34] Bean K E 1978 *IEEE Trans. Electron Devices* **25** 1185–93
[35] Dobrovinskaya E R, Lytvynov L A and Pishchik V 2009 *Properties of Sapphire* (Boston, MA: Springer)
[36] Properties of sapphire (available at: www.mt-berlin.com/frames_cryst/descriptions/sapphire.htm) (Accessed 12 January 2021)
[37] Borchardt-Ott W 2012 *Crystallography* (Berlin: Springer)
[38] Hubbard T J 1994 MEMS design: the geometry of silicon micromachining *PhD Thesis* California Institute of Technology (https://thesis.library.caltech.edu/3565/1/Hubbard_tj_1994.pdf)
[39] Siem E J and Carter W C 2005 *J. Mater. Sci.* **40** 3107–13
[40] Salvalaglio M, Backofen R, Bergamaschini R, Montalenti F and Voigt A 2015 *Cryst. Growth Des.* **15** 2787–94

[41] Albani M, Bergamaschini R, Salvalaglio M, Voigt A, Miglio L and Montalenti F 2019 *Phys. Status Solidi* b **256** 1800518
[42] Zubel I 2019 *J. Micromech. Microeng.* **29** 093002
[43] Du D, Srolovitz D J, Coltrin M E and Mitchell C C 2005 *Phys. Rev. Lett.* **95** 155503
[44] Silvaco Victory Process (https://silvaco.com/tcad/) (Accessed 12 January 2021)
[45] De Graef M and McHenry M E 2012 *Structure of Materials: An Introduction to Crystallography, Diffraction and Symmetry* 2nd edn (Cambridge: Cambridge University Press)